

# Advanced FVTD Simulation of Dielectric Resonator Antennas and Feed Structures

Christophe Fumeaux, Dirk Baumann, Rüdiger Vahldieck  
 Swiss Federal Institute of Technology, ETHZ, IFH, 8092 Zürich, Switzerland  
 E-mail: fumeaux/dbaumann/vahldieck@ifh.ee.ethz.ch

**Abstract**—This paper illustrates the application of the Finite-Volume Time-Domain (FVTD) method to the electromagnetic modeling of complex 3D antenna structures. The FVTD algorithm solves Maxwell's equations in a conformal polyhedral mesh, therefore permitting an accurate approximation of curved surfaces and a fine resolution of structural details. The flexibility of the unstructured mesh is coupled with a geometry-matched local time-stepping scheme to increase the computational efficiency. The FVTD algorithm is applied here to simulate probe-fed hemispherical dielectric resonator antennas. Emphasis of the investigation is placed on the modeling of fabrication details and their influence on the input impedance and resonance frequency of the device.

**Index Terms**—3D FVTD method, conformal meshing, dielectric resonator antenna

## I. INTRODUCTION

The Finite-Volume Time-Domain (FVTD) method has been introduced at the end of the 1980's [1], [2] as a powerful technique for numerically solving Maxwell's equations in unstructured meshes. Typically, the FVTD algorithm is applied in a tetrahedral mesh, therefore avoiding stair-casing approximations for the discretization of curved or non-orthogonal surfaces. The FVTD method stands therefore as an alternative to the Finite-Difference Time-Domain (FDTD) method for complex geometries where conformal meshing is advantageous.

Another important characteristic of unstructured meshes is their ability to adapt the cell size to the local geometrical requirements. Since the transition between domains with different feature sizes can be made very fast, the number of cells in the computational domain can be minimized without sacrificing the resolution. Modeling small structural details, e.g. the feed of an antenna, in close proximity to large structures is a frequently encountered practical problem. A solution to this problem strongly benefits from different scales of cell sizes: In the coarse regions of the problem, the standard linear cell dimension will be determined by a fraction of the shortest wavelength of interest (typically  $\lambda/10$ ), whereas resolution of details might require much smaller cell dimensions (e.g. in the order of  $\lambda/100$  or smaller). Another advantage of inhomogeneous meshes consists in the modeling of boundaries between materials with a large dielectric contrast. The shorter wavelength in the denser material

requires finer cell sizes than in free-space, which can be achieved straightforwardly in an unstructured tetrahedral mesh. Since the FVTD method keeps the number of needed cells to a minimum in complex problems, it saves memory despite a computationally higher expense for a single cell (geometrical data are required) compared to FDTD.

Simulations of dielectric resonator antennas (DRA) are very challenging problems that can take advantage of the geometrical flexibility of the FVTD method: A DRA typically includes curved boundary surfaces with a large dielectric contrast, and small feeding mechanisms. In this investigation, a hemispherical DRA fed by a coaxial probe is modeled. The effects of different probe configurations and of fabrication imperfections are studied numerically. The results demonstrate the versatility of the FVTD technique.

## II. THE FVTD ALGORITHM

The FVTD method is based on Maxwell's equations written in conservative form and integrated over elementary volumes [3]. The implementation in a digital computer requires the approximation of the equations in each elementary volume of a given spatial grid. In a tetrahedral mesh, each volume  $V_i$  has 4 faces with areas  $F_k$  and outward-pointing unit normal vector  $\vec{n}_k$ . This yields the following vector equations

$$\begin{aligned} -\mu V_i \frac{\partial}{\partial t} \langle \vec{H} \rangle_{V_i} &= \sum_{k=1}^4 \left( \vec{n}_k \times \langle \vec{E} \rangle_{F_k} \right) F_k \\ \epsilon V_i \frac{\partial}{\partial t} \langle \vec{E} \rangle_{V_i} &= \sum_{k=1}^4 \left( \vec{n}_k \times \langle \vec{H} \rangle_{F_k} \right) F_k \end{aligned} \quad (1)$$

The left-hand side (LHS) of (1) represents a volume integral, where the triangular brackets denote the averaging of the field components over the considered volume. This average is approximated by the value of the fields in the barycenter of the tetrahedron. The right-hand side (RHS) of (2) represents a sum of surface integrals over the faces of the considered finite volume. The integrands are so-called (mathematically defined) "fluxes" through the faces of the cells. The triangular brackets represent the averaging of the fields over each face of the tetrahedron. The approximation locates the average field components in the barycenter of the considered face.

The interaction between adjacent cells in the FVTD algorithm happens, as inspired by FV techniques in fluid

dynamics, through separation of the flux terms in incoming (-) and outgoing (+) contributions (split-flux formulation [3])

$$\begin{aligned}
 -\mu V_i \frac{\partial}{\partial t} \langle \vec{H} \rangle_{V_i} &= \sum_{k=1}^4 \left( \vec{n}_k \times \langle \vec{E} \rangle_{F_k}^+ - \vec{n}_k \times \langle \vec{E} \rangle_{F_k}^- \right) F_k \\
 \varepsilon V_i \frac{\partial}{\partial t} \langle \vec{E} \rangle_{V_i} &= \sum_{k=1}^4 \left( \vec{n}_k \times \langle \vec{H} \rangle_{F_k}^+ - \vec{n}_k \times \langle \vec{H} \rangle_{F_k}^- \right) F_k
 \end{aligned} \quad (2)$$

Explicit update equations for the fields in the finite volumes are obtained by discretizing the time variable in (2). Different time-marching schemes can be applied for this purpose. In a first-order approximation, the  $\partial/\partial t$  is estimated using a finite difference. In the algorithm implemented for this study, the second-order Lax-Wendroff predictor-corrector scheme [3] is used. A significant increase of the efficiency of the FVTD march-in-time iteration is obtained through the application of geometry-matched local time steps [4].

### A. Local Time Steps

The local time step technique is based on a special partition of the computational domain into sub-domains. This partition is performed automatically during preprocessing based on local geometric and material conditions of the elements in the mesh. To obtain a robust and precise local time step scheme, three restrictions are set on the sub-domain partition:

- 1) The partition defines only discrete levels of local time steps that correspond to power of two times  $\Delta t$  ( $\Delta t, 2\Delta t, 4\Delta t, 8\Delta t, \dots$ ), where  $\Delta t$  is the fundamental time step that assures stability in the whole mesh.
- 2) The time steps of two adjacent sub-domains must have a ratio of two. Thus, multiple scale problems produce nested sub-domains.
- 3) The local time step for all elements in each sub-domain satisfies the stability condition.

A division of the computational domain satisfying these three conditions is performed using an iterative process described in [4]. The restrictions imposed on the partition allow a treatment of the borders between sub-domains as generic two-level boundaries, which are inserted very naturally in the FVTD march-in-time iteration. The time consistency is preserved by introducing an artificial half-step in the larger cells of a time-step boundary. The principle is demonstrated in Fig. 1 for first-order march in time. A boundary between the first and the second level of time step is depicted, but the procedure is similar for all other time step levels. The values of the fields in the higher level boundary cell are required at time step  $n+1$  to perform the second small time step (③, from  $n+1$  to  $n+2$ ) in the lower level cell. Since the fields at this time step are not computed explicitly in the large cells, these values are obtained through averaging the fields computed at time steps  $n$  and  $n+2$  (operation denoted by ②). It is therefore necessary to perform the update of the larger cell (①a from  $n$  to  $n+2$ ) before the second update in the smaller cell (③, from  $n+1$  to  $n+2$ ). The technique is described here for a first-order time discretization but can be extended to more sophisticated schemes as shown in [4].

The less frequent update of larger cells in the mesh allows a significant speedup of the computations when different element scales are present in the simulated structures. Although the update of a cell at the boundary between sub-domains requires around two times more CPU time than a standard cell at the same time-step level, this does not slow down the computation significantly since boundary cells represent only a few percent of the total number of cells.

The local time step scheme used in this study has proven to be very accurate and robust since it requires no space interpolation and only simple time interpolations. Therefore, the fundamental time step does not require a more severe stability condition than the original algorithm. This has been confirmed in all examples computed in practice, involving up to 8 nested levels of time steps (from  $\Delta t$  to  $256\Delta t$ ).

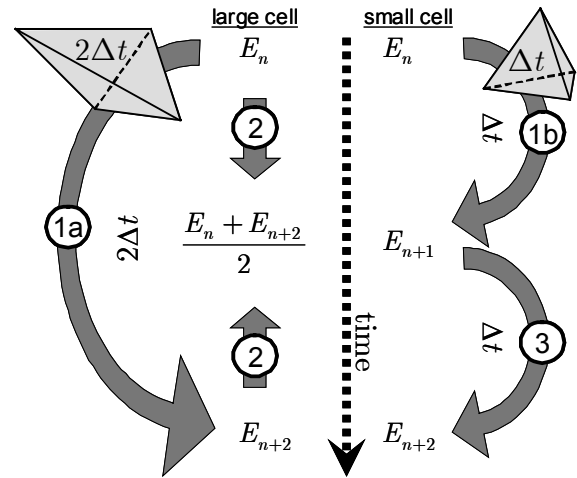


Fig. 1. Principle of application for local time steps at the boundary between sub-domains (two-level system). The chronology is indicated by the encircled numbers. An artificial half-step ② is created in the large cell to obtain data required to perform the update ③.

### B. Near-Field to Far-Field Transformation

The far-field patterns are computed using a Huygens' surface enclosing the antenna. This triangulated closed surface is embedded in the tetrahedral mesh. A discrete Fourier transformation (DFT) is performed on the fly during the FVTD iteration to obtain the necessary frequency-domain tangential fields in the center of each triangle of the Huygens' surface. The sampling frequency of the DFT is determined by the local time step of the sub-domain where the sampled fields are located.

### C. Ports

Port planes are introduced as triangulated surfaces in the FVTD mesh. The planes force the tetrahedrons to be aligned with respect to one face and therefore form a phase reference plane for the incident and the reflected waves.

The flux-splitting formulation in (2) is exploited to compute the incident and the reflected fields in a port plane consisting of  $N$  triangles. This allows to directly calculate power waves without the need to determine voltages and currents in the port by [5].

$$a(n)^2 = \sum_{k=1}^N (\mathbf{E}_t^+(k, n) \times \mathbf{H}_t^+(k, n)) F_k \quad (3)$$

$$b(n)^2 = \sum_{k=1}^N (\mathbf{E}_t^-(k, n) \times \mathbf{H}_t^-(k, n)) F_k$$

where the subscript  $t$  denotes tangential fields and the superscripts  $+$  and  $-$  indicate incident and reflected fields. In a multimode environment the total field in a waveguide can be expressed as a sum over all possible modes. Due to the orthogonality of the modes, the mode amplitude of each mode can be determined. Thus the amplitude  $A_m^{+/-}(n)$  of the  $m$ th mode at time step  $n$  can be computed with

$$A_m^{+/-}(n) = \sum_{k=1}^N \mathbf{E}_t^{+/-}(k, n) \cdot \mathbf{e}_m(k) F_k \quad (4)$$

if the normalized mode template vector  $\mathbf{e}_m$  is known a priori. The power waves can then be computed as

$$a = A^+ / \sqrt{Z_w}$$

$$b = A^- / \sqrt{Z_w} \quad (5)$$

with  $Z_w$  being the wave impedance.

### III. THE HEMISPHERICAL DIELECTRIC RESONATOR ANTENNA

Dielectric resonators placed in an open environment can be used as radiating elements showing such attractive characteristics as small size, large bandwidth, high efficiency and simplicity of excitation [6]. Numerous shapes of resonators have been used including rectangles, cylinders, rings and hemispheres. The coupling of power to the dielectric structure can be achieved through coaxial probes, apertures, microstrip, or coplanar lines. Most of the designs exhibit a large dielectric contrast to free-space and at the same time small feed dimensions. The FVTD method seems therefore perfectly suited to investigate this class of antennas.

To illustrate the advantages of the FVTD simulations, a hemispherical probe-fed dielectric resonator antenna with characteristics close to the devices presented in [7] and [8] is chosen. The geometry is depicted in Fig. 2 showing all the relevant dimensions. The feed configuration excites the  $TE_{111}$  mode of the DRA with a resonant frequency in the vicinity of 3.6 GHz. The results of the FVTD simulations have been compared previously [9] with those of a finite-element based commercial program, showing a good agreement for return loss and radiation patterns. The ground plane is chosen as a circular plate with a radius of 60 mm. The present paper investigates the influence of small details on the characteristics of the device. The resolution of fine features in the simulation yields useful information on the effects of fabrication tolerances that might cause discrepancies from predictions of simplified idealized models. In the following, the effect of the probe shape and length, as well as the influence of air gaps around the probe or between the ground plane and the dielectric will be investigated numerically using the FVTD method.

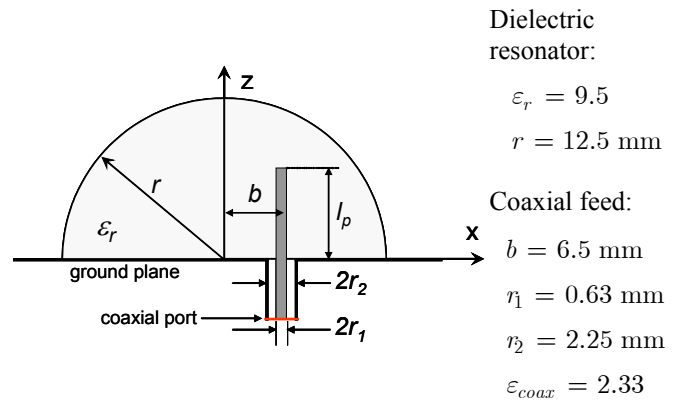


Fig. 2. Schematic cross section of the probe fed hemispherical DRA.

#### A. General Characteristics of the FVTD Model

The broadband simulation is performed in the frequency range from 3 GHz to 6 GHz. The computational domain is closed by a sphere with radius of 80 mm where a Silver-Müller absorbing boundary condition is applied.

The fineness of the mesh is adapted to the different parts of the devices as shown in Table I and Fig. 3. The resulting ratio of volumes  $V_{\max}/V_{\min}$  in the mesh reaches typically more than 100'000. For an efficient simulation, this spatial inhomogeneity of the mesh is coupled to an inhomogeneous time discretization with up to seven levels of local time steps ( $64\Delta t$ ). A cut through a meshed model is depicted in Fig. 3 showing typical linear cell dimensions associated to different regions of the considered DRA problem. The mesh around the probe is determined by the geometrical resolution desired and might be even finer when an air gap needs to be resolved. The transitions between the different regions of the mesh are smooth in nature in the tetrahedral mesh.

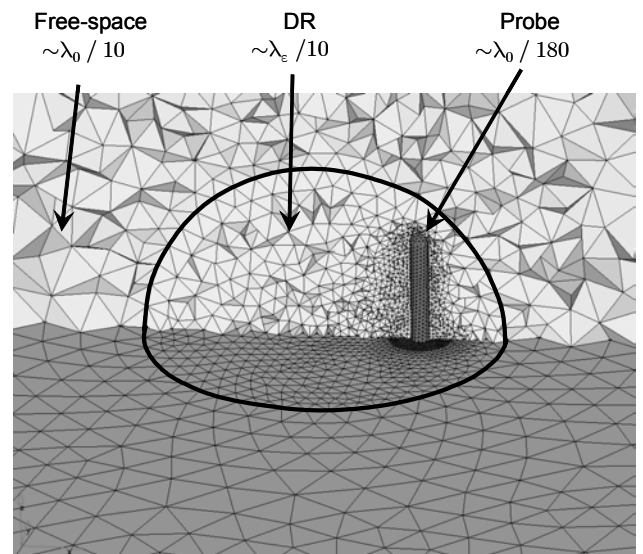


Fig. 3. Cut through the 3D model of the DRA showing the mesh with different fineness adapted to the local geometry. The maximal ratio of volumes in the associated tetrahedral mesh reaches more than 100,000. The presence of thin air gaps in other models results in even larger size contrasts.

TABLE I

TYPICAL LINEAR DIMENSIONS OF THE TRIANGLES USED FOR THE SURFACE DISCRETIZATIONS. THE FINENESS OF THE VOLUME MESH IS DETERMINED BY THE SURFACE DISCRETIZATION. THE NUMBERS IN TERMS OF WAVELENGTHS ARE GIVEN RELATIVE TO THE SHORTEST WAVELENGTH OF INTEREST (I.E., AT 6 GHz).

	Linear dimensions		
	absolute	in terms of $\lambda_0$	in terms of $\lambda$
Outer boundary	6 mm	$\lambda_0 / 8.3$	$\lambda_0 / 8.3$
DRA surface	1.6 mm	$\lambda_0 / 31.5$	$\lambda_\epsilon / 10$
Probe feed	0.28 mm	$\lambda_0 / 180$	$\lambda_{coax} / 117$
Thinnest air gap (0.05 mm)	0.05 mm	$\lambda_0 / 1000$	$\lambda_0 / 1000$

### B. Detailed Model of the Coaxial Probe

The simulations of the hemispherical DRA have been performed for a set of different probe lengths  $l_p$  between 1.0 mm and 9.5 mm. The variation of the probe length is a practical way of controlling the input impedance of the DRA. In addition to varying the length, detailed configurations of the probe have been investigated in the frame of this study. Different generic cases are represented in Fig. 4. The probe of the first case (Fig. 4 (a)) is a cut wire with an abrupt end, whereas the probe of the second case (Fig. 4 (b)) has a rounded tip. In the third case, an air gap exists between the probe (rounded tip) and the dielectric material (Fig. 4 (c)). Different thicknesses of air gaps between 0.05 and 0.30 mm have been modeled. All configurations have been considered from the perspective of the matching to  $50 \Omega$  and from the point of view of the resonant frequency of the DRA. The return loss is a practical value for a specific matching condition but does not yield full information on the exact location of the resonant frequency.

The presence of a thin air gap around the probe requires a finer mesh around the probe than corresponding simulations without air gap. Typical ratios of volumes  $V_{\max} / V_{\min}$  are given in Table II for different thicknesses of air gap.

### C. Effect of Local-Time Stepping

The local time stepping permits to achieve a significant speedup of the simulation since the large cells in the mesh will

TABLE II  
MESH CHARACTERISTICS FOR DIFFERENT MODELS WITH AIR GAP AROUND THE PROBE. THE THICKNESS OF THE AIR GAP IS GIVEN IN MILLIMETER.

Model	# of cells	$V_{\max} / V_{\min}$	Top level
Air Gap 0.05	379,657	3,675,074	7 ( $64 \Delta t$ )
Air Gap 0.10	237,213	803,117	7 ( $64 \Delta t$ )
Air Gap 0.20	212,859	117,411	5 ( $16 \Delta t$ )
Air Gap 0.30	213,379 *	95,011	5 ( $16 \Delta t$ )
No air gap	209,443	112,652	5 ( $16 \Delta t$ )

\* The number of elements for air gap 0.20 and 0.30 is very similar since the discretization used on the probe (0.28 mm, Table I) is sufficient to resolve both gap dimensions.

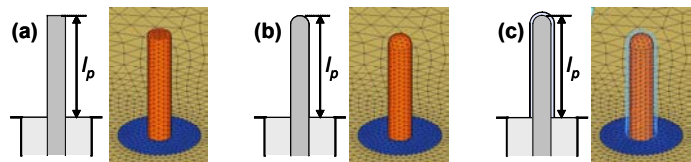


Fig. 4. Different models of the probe: (a) probe with cut end, (b) probe with a rounded tip, (c) probe with a rounded tip and an air gap.

be updated much less often than the small ones. For the type of problems presented here, computation speedup factors of 4 to 10 are achieved using this technique compared to the corresponding simulations performed without local time stepping. The largest speedups are achieved for the most inhomogeneous meshes.

The influence of the local time stepping on the simulation result has been demonstrated to be negligible [4]. In the practical examples presented here, the same conclusions can be applied. As illustration, the field amplitude in one particular point is represented in Fig. 5 together with the difference of the computed values obtained with and without local time stepping. Even when five to seven nested local time-step sub-domains are used, the discrepancies are well below -50 dB.

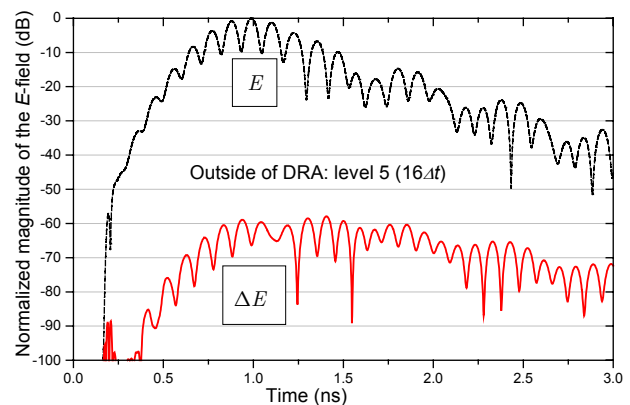


Fig. 5. Influence of the local time stepping on the amplitude of the electric field at a point located outside the DRA. The arbitrarily chosen point is updated with a local time step corresponding to 16 times the fundamental time step. The upper curve ( $E$ ) shows the E-field magnitude in this point and the lower curve ( $\Delta E$ ) the difference between the simulations performed with and without local time stepping.

#### IV. DETAILED SIMULATION OF THE DRA

In this section, several features of the probe-fed DRA are investigated. After a general analysis of the effect of the probe length, the emphasis is placed on the modeling of details that might arise from fabrication imperfections [10].

##### A. Probe Length Dependence

The variation of the probe length represents a very convenient way to control the input impedance of the probe-fed DRA [7]. The return loss of the DRA fed by a 50  $\Omega$  coaxial line is represented for probe length  $l_p$  between 5 and 9 mm in Fig. 6. The optimum matching of the antenna for the first resonance located around 3.6 GHz (TE<sub>111</sub> mode) is obtained for a probe length between 7 mm and 8 mm. Higher-order resonances with different optimum probe lengths are observed around 5.3 GHz and 5.7 GHz (Fig. 7).

These results have been obtained using probes with cut ends (Fig. 4 (a)). The following paragraphs investigate the influence of probe details on the matching condition.

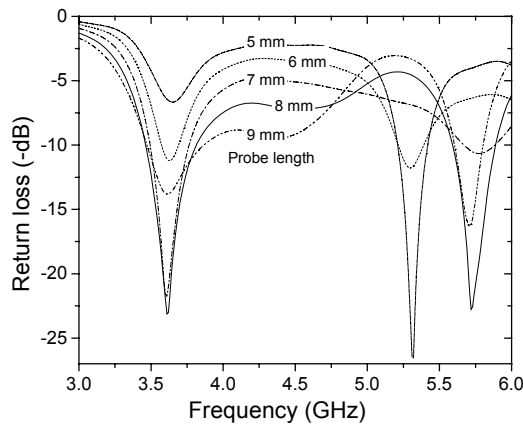


Fig. 6. Return loss (related to 50  $\Omega$  coaxial cable feeding) as a function of the frequency for different probe lengths. The probes used in the models have a cut end.

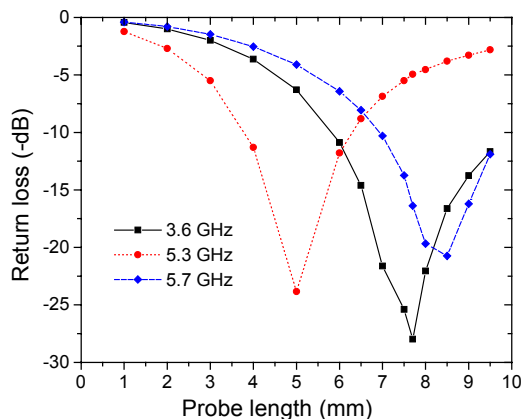


Fig. 7. Return loss as a function of the probe length at three different frequencies.

##### B. Effect of Rounded Probe Tip

Rounding the tip of the probe makes it appear electrically slightly shorter than a cut-end probe with the same length. This has an influence on the matching of the device and is best

observed on the return loss curves. On the upper graph of Fig. 8, the return loss for a rounded probe with length 6.5 mm remains for all frequencies in between curves for cut-end probes with length 6.0 mm and 6.5 mm. This suggests an "effective length" for the rounded probe between 6.0 mm and 6.5 mm. This particular example has been chosen for illustration since it also shows a higher resonance close to 5.3 GHz. Similar observations are made for all probe lengths.

The lower graph of Fig. 8 considers lengths closer to an optimal matching for 50  $\Omega$  and permits to quantify how shorter a rounded tip appears: The return loss of a rounded probe with 8 mm is nearly identical to the one of a cut-end probe with length 7.7 mm. This reduction corresponds roughly to half the radius of the rounding. Similar conclusions can be drawn for all probe lengths.

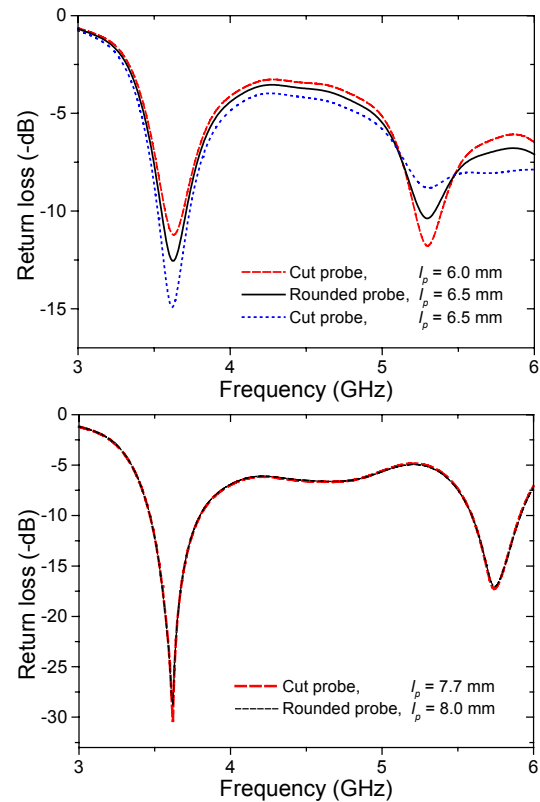


Fig. 8. Return loss for the probe-fed hemispherical resonator for different probe lengths illustrating the reduction of effective length caused by rounding the tip of the probe. Upper graph: The curve for rounded probe with 6.5 mm length is located in between the probes with lengths 6.0 mm and 6.5 mm. Lower graph: Nearly identical curves are obtained when considering a rounded tip 0.3 mm longer (here close to optimal length of the probe).

##### C. Effect of Air Gap around the Probe

The presence of an air gap around the probe has a more pronounced effect on the matching condition of the device than the rounding of the tip, since it basically alters the boundary condition over the whole surface of the probe. This has been investigated experimentally in [11] showing a significant effect of air gaps around the probe which fed a cylindrical dielectric resonator. Such an air gap might exist because of the mechanical tolerances associated with drilling a hole in the dielectric material to insert the probe.

In the present numerical study, we have used the FVTD method to model air gaps around the probe of the hemispherical DRA. Different thicknesses of air gap between 0.05 mm and 0.3 mm have been modeled and compared to the ideal case of a perfect mechanical contact between the probe and the dielectric (no air gap).

The input impedance of the probe-fed hemispherical DRA (rounded probe with length 8.0 mm) is plotted in Fig. 9 close to the first resonance frequency for different values of the air gap. The presence of the air gap shifts the peak of the input resistance towards higher frequencies and lowers its maximum value. Very thin air gaps can lower significantly the magnitude of the peak input resistance. The largest air gap modeled here (0.3 mm) roughly reduces the maximum input resistance to half (from 59  $\Omega$  to 25  $\Omega$ ) and moves its location from 3.56 GHz to 3.67 GHz. A similar behavior is observed for the higher-order resonances.

Results from a simulation neglecting such air gaps would not yield accurate design parameters. This can be explicitly observed in Fig. 10 where the return loss is represented around the first resonance for several thicknesses of the air gap. A qualitatively similar behavior has been observed experimentally in [11] for a cylindrical DRA.

From the point of view of the computational cost, the resolution of very thin air gaps (e.g. here 0.05 mm) around the

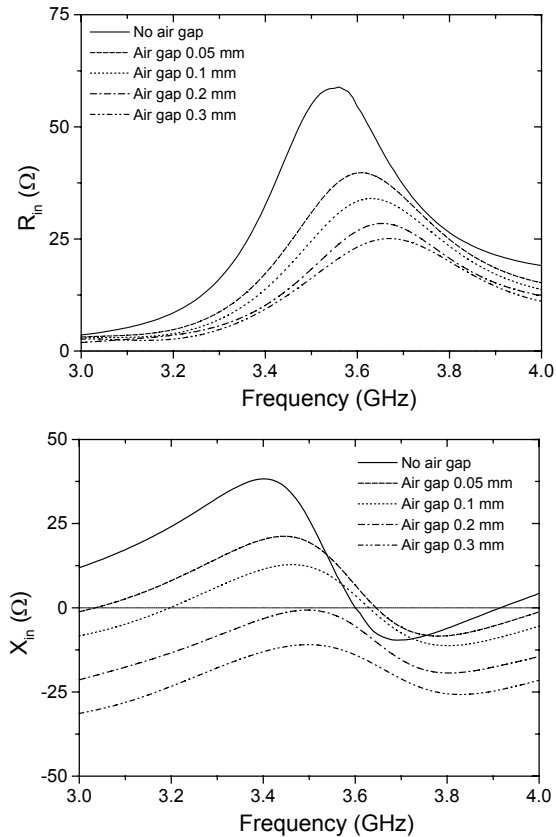


Fig. 9. Effect of an air gap surrounding the probe on the input impedance  $Z_{in}$  of the DRA. The rounded probe has a length of 8.0 mm. The  $R_{in}$  (upper graph) and  $X_{in}$  (lower graph) indicate the real and imaginary part of the input impedance respectively.

probe typically increases the number of cells in the mesh (Table II) and therefore the overall computational effort. Introducing local time-steps dampens this negative effect since the necessary reduction of time steps associated with the small cells affects only a limited region around the feed.

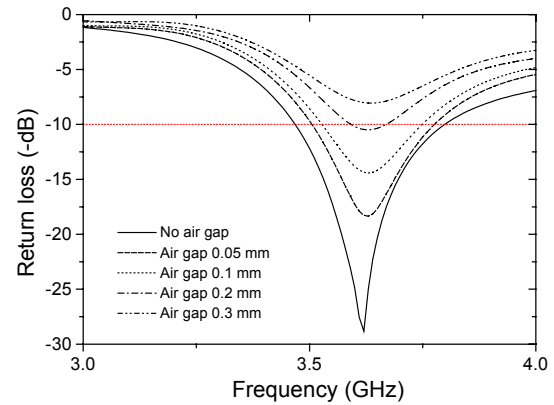


Fig. 10. Return loss of the hemispherical DRA with different thicknesses of air gap around the probe. The figure illustrates the degradation of the matching condition that can occur because of fabrication tolerances.

#### D. Effect of Air Gap between DRA and Ground Plane

Another fabrication issue likely to affect the radiation characteristics of a DRA has been described in [12]: A thin gap between the dielectric material and the ground plane can affect severely the input impedance of the device. This can be explained by a change in boundary condition at the bottom of the DRA.

The effect of the air gap between the hemispherical DRA and the ground plane on the input impedance is shown in Fig. 11 for different thicknesses of air gap (0.15 mm, 0.30 mm and 0.45 mm). The results are compared to the corresponding device without air gap. It is obvious that the presence of the air gap shifts the resonance frequency and the peak of the input resonance upwards in a significant manner. This can be interpreted as a lowering of the effective dielectric constant of the DRA due to the presence of the air gap.

The shift in resonance frequency shown in Fig. 11 is associated to a decrease of the Q factor of the structure and to an increase of the matching bandwidth of the device. As illustration of this fact, the return loss of the four DRAs is shown in Fig. 12. The relative bandwidth is doubled through the presence of the 0.3 mm air gap between the dielectric resonator and the ground plane. The exploitation of this effect has been suggested in [10] as a practical means to increase bandwidth. The downside of the technique is a required increase in size of the device for a fixed frequency of operation.

From the point of view of the computational effort, it should be mentioned again that resolving very thin gaps increases the overall number of cells in the computational domain. The type of air gap considered here has a more pronounced effect on the computational load since larger regions of the computational domain are affected than in the case of the air gap around the probe.

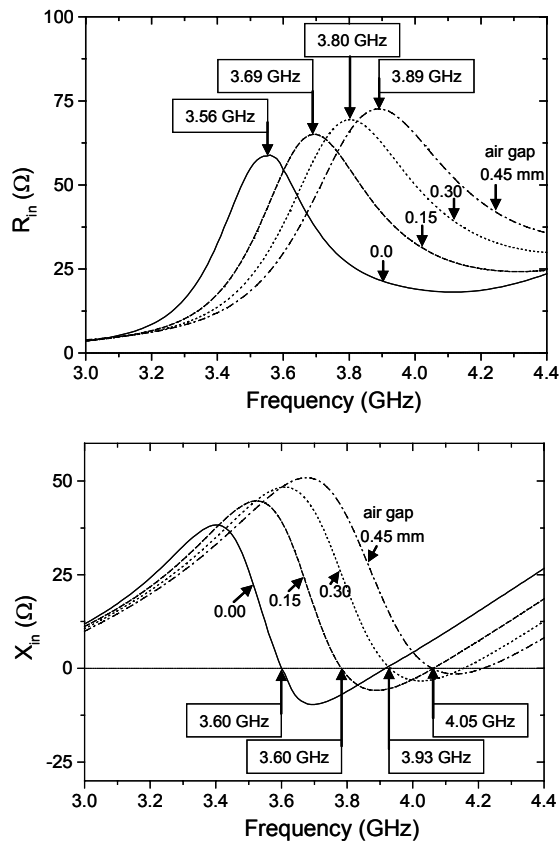


Fig. 11. Effect of an air gap between DRA and ground plane on the input impedance  $Z_{in}$  of the DRA. The rounded probe has a length of 8.0 mm. The  $R_{in}$  (upper graph) and  $X_{in}$  (lower graph) indicate the real and imaginary part of the input impedance respectively.

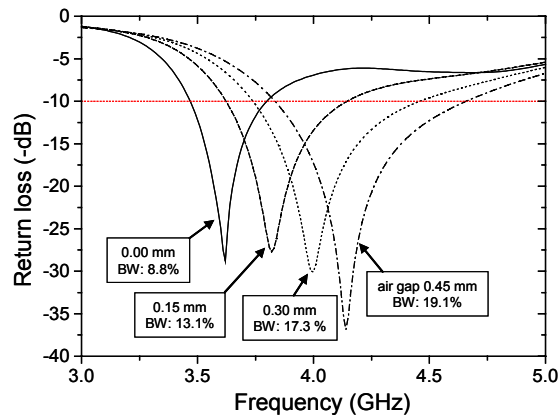


Fig. 12. Return loss of the hemispherical DRA with different air gaps between the dielectric and the ground plane. The figure illustrates the shift of the resonance frequency and the increase of the relative bandwidth when the air gap becomes thicker.

**E. Effect of the Feeding on the Radiation Pattern**

The radiation pattern is mainly determined by the geometry of the dielectric material and by the arrangement of the ground plane. However, by changing the location of the probe inside the DRA, different modes might be excited in the dielectric, leading to different radiation patterns. In the simulations presented here, the location of the probe has been kept

constant at a distance of 6.5 mm from the center of the hemisphere. This arrangement is chosen for excitation of the  $TE_{111}$  mode inside the dielectric.

For all the simulations where only the probe has been modified (as in paragraphs A, B, and C), no relevant variations of the patterns have been observed for any probe length or shape. This confirms that the variations of the probe represent a practical way of matching the antenna to the feed circuit without changing the radiation characteristics.

On the contrary, small differences can be observed if the relative arrangement of the ground plane and the DRA is modified. This is the case for example when the air gap is introduced between dielectric and ground plane (Paragraph D).

In Fig. 13, the computed patterns of the DRA are shown at a frequency of 3.6 GHz (near first resonance) in two principal planes. The curves are represented for three different configurations. The first two models chosen (curves 1 & 2) have different feeds (1 mm cut probe, and 8 mm rounded probe with air gap) and their patterns cannot be distinguished, even though the input impedances of the devices are very different. The third curve shown in the figure represents a DRA that has an additional air gap (0.45 mm thick) between the dielectric and the ground plane. This affects the patterns of the device, although not dramatically.

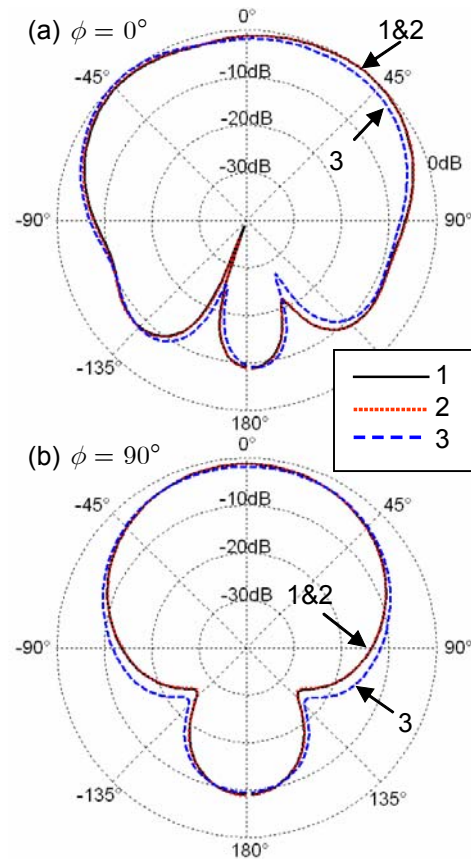


Fig. 13. Radiation patterns of the DRA at 3.6 GHz in two principal planes: (a) plane containing the probe (E-plane), (b) orthogonal plane (H-plane). The patterns are represented for three configurations: (1) 1 mm cut probe, (2) 8 mm rounded probe with 0.3 mm air gap around the probe, (3) 8 mm rounded probe plus air gap between the ground plane and the dielectric.

*F. Effect of the Finite Ground Plane*

A more visible effect can be observed when the dimensions of the ground plane of the DRA are changed. Different sizes of ground planes on the bottom of the dielectric have been modeled. Results for planar circular ground planes with radii equal to 60 mm and 180 mm have been compared to those with infinite ground plane. Modeling the latter, a perfectly conducting symmetry plane has been used in conjunction with image theory during the near to far field transformation necessary to obtain the radiation patterns.

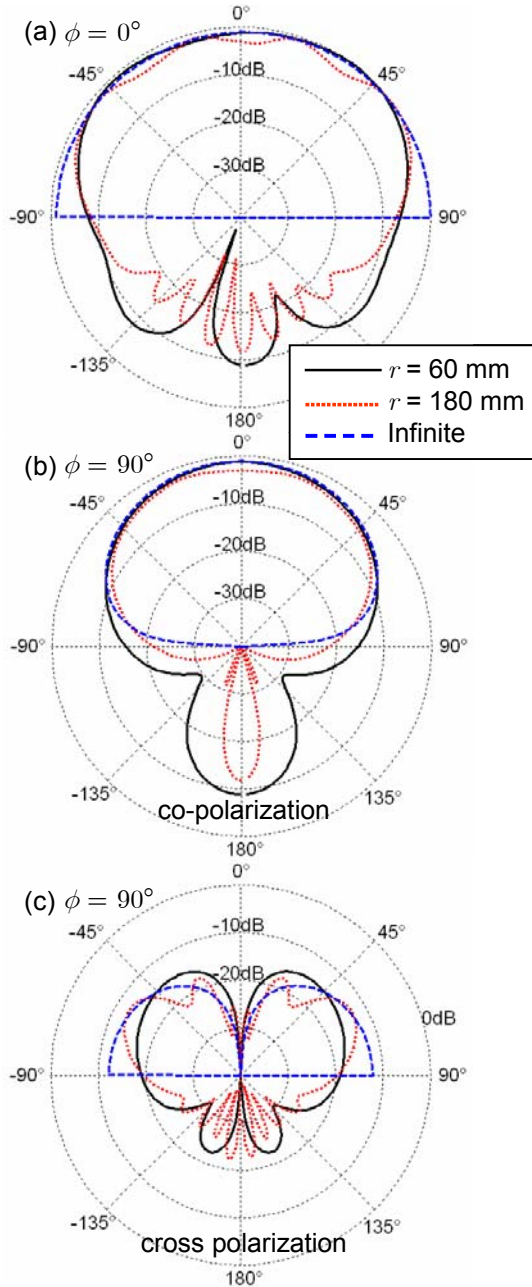


Fig. 14. Radiation patterns near the first resonance (3.6 GHz) for the hemispherical DRA with rounded probe (length 8 mm). The different curves correspond to the given radii  $r$  of the circular ground plane. (a) E-plane co-polarized pattern  $E_\theta$ , (b) H-plane co-polarized pattern  $E_\phi$ , (c) H-plane cross-polarized pattern  $E_\theta$ . The cross-polarized component in the E-plane is too small to be represented in this scale.

From the point of view of matching the DRA to the feed circuit, the use of different ground planes does not have a noticeable effect. On the other hand, we observe that the radiation patterns are clearly influenced by the extent of the ground plane. The angular patterns in two principal planes are shown in Fig. 14 and Fig. 15 for the cross- and co-polarized components (third Ludwig definition [13]) of the radiated fields at the first two resonances. The cross-polarized component in the E-plane (plane containing the probe) is not shown since it is negligibly small.

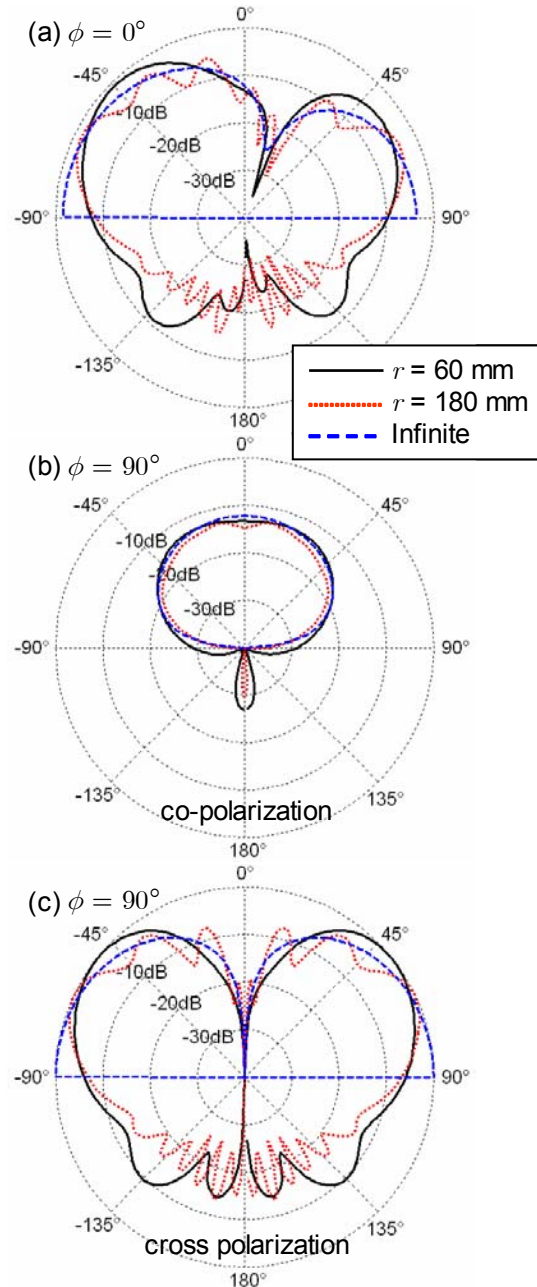


Fig. 15. Radiation patterns near the second resonance (5.3 GHz) for the hemispherical DRA with rounded probe (length 8 mm). The different curves correspond to the given radii  $r$  of the circular ground plane. (a) E-plane co-polarized pattern  $E_\theta$ , (b) H-plane co-polarized pattern  $E_\phi$ , (c) H-plane cross-polarized pattern  $E_\theta$ . The cross-polarized component in the E-plane is too small to be represented in this scale.

Comparing the radiation patterns at the two frequencies (Fig. 14 vs. Fig. 15), it can be observed that the first resonance radiates towards broadside whereas the second radiates with end-fire characteristics.

The chosen sizes of the ground planes correspond to diameters larger than the free-space wavelength at the first resonance ( $1.45 \lambda_0$  and  $2.17 \lambda_0$  respectively at 3.6 GHz). We observe small oscillations of the curves (local maxima and minima) as a function of the angle for the finite ground planes. These oscillations are caused by resonances of the ground plane, which is confirmed by the fact that the device with three times larger ground plane have three times faster angular oscillations (see e.g. the back lobes). It is also observed as expected that the back radiation is reduced when the ground plane is extended.

These simulations show qualitatively the errors that arise when using infinite ground-plane computations to model devices with relatively small ground planes.

## V. CONCLUSIONS

The FVTD method has been applied to the simulation of a probe-fed hemispherical DRA. Emphasis of the investigation has been placed on the effect of manufacturing issues, such as influence of feeding details on the matching and on the resonance frequency. The probe length provides as expected a convenient way to match the device to the circuit with a negligible influence on the radiation pattern. The shape of the probe tip has been demonstrated to have a sensible effect on the input impedance of the device: A rounded probe appears shorter than a cut probe. A more pronounced effect is introduced by an air gap between the probe and the dielectric material: The input impedance is significantly lowered and the resonance is shifted toward larger frequencies.

The simulations presented here demonstrate the versatility of the FVTD algorithm. Modeling other complex shapes (e.g. [14],[15]) does not change or increase the complexity level of the algorithm. The intrinsic geometrical flexibility of the method permits, when coupled to a local time-stepping scheme, the resolution of small details with excellent accuracy. This makes the FVTD method a very powerful tool that can be applied to assess the effect of fabrication tolerances of complex devices.

## ACKNOWLEDGMENT

This work was supported by the Swiss procurement agency (armasuisse), Bern, Switzerland.

## REFERENCES

- [1] N. K. Madsen, R. W. Ziolkowski, "A three-dimensional modified finite volume technique for Maxwell's equations", *Electromagnetics*, vol. 10, pp. 147-161, 1990
- [2] V. Shankar, A. H. Mohammadian, W. F. Hall, "A time-domain, finite-volume treatment for the Maxwell equations", *Electromagnetics*, vol. 10, pp. 127-145, 1990
- [3] P. Bonnet, X. Ferrieres, B. L. Michielsen, P. Klotz, J. L. Roumiguieres, "Finite-Volume Time Domain Method", Chapter 9 in *Time domain electromagnetics*, edited by S. M. Rao, Academic Press, San Diego, 1999
- [4] C. Fumeaux, D. Baumann, P. Leuchtman, R. Vahldieck, "A generalized local time-step scheme for efficient FVTD simulations in strongly inhomogeneous meshes", *IEEE Trans. Microwave Theory Tech.* MTT-52(3), pp. 1067-1076, 2004
- [5] D. Baumann, C. Fumeaux, P. Leuchtman, R. Vahldieck, "Generalized-scattering-matrix extraction using the finite-volume time-domain (FVTD) method", *IEEE MTT-S Int. Microwave Symp. Dig.*, pp. 1701-1704, June 2004
- [6] A. Petosa, A. Ittipiboon, Y. M. M. Antar, D. Roscoe, M. Cuhaci, "Recent advances in dielectric-resonator antenna technology", *IEEE Antennas Propagat. Mag.* 40(3), pp. 35-48, 1998
- [7] K. W. Leung, K. M. Luk, K. Y. A. Lai, D. Lin, "Theory and experiment of probe fed dielectric resonator antenna", *IEEE Trans. Antennas Propagat.* AP-41, pp. 1390-1398, 1993
- [8] K. W. Leung, K. K. Tse, K. M. Luk, E. K. N. Yung, "Cross-polarization characteristics of a probe-fed hemispherical dielectric resonator antenna", *IEEE Trans. Antennas Propagat.* AP-47(7), pp. 1228-1230, 1999
- [9] D. Baumann, C. Fumeaux, P. Leuchtman, R. Vahldieck, "Finite-Volume Time-Domain (FVTD) Method and its Application to the Analysis of Hemispherical Dielectric-Resonator Antennas", *IEEE MTT-S Int. Microwave Symp. Dig.*, pp. 985-988, June 2003
- [10] G.P. Junker, A.A. Kishk, A.W. Glisson, D. Kajfez, "Effect of fabrication imperfections for ground-plane-backed dielectric-resonator antennas", *IEEE Antennas Propagat. Mag.* 37(1), pp. 40-47, Feb. 1995
- [11] G. P. Junker, A. A. Kishk, A. W. Glisson, D. Kajfez, "Effect of an air gap around the coaxial probe exciting a cylindrical dielectric resonator antenna", *Electronics Letters* 30(3), pp. 177-178, 1994
- [12] G. P. Junker, A. A. Kishk, A. W. Glisson, D. Kajfez, "Effect of an air gap on a cylindrical dielectric antenna operating in the  $TM_{01}$  mode", *Electronics Letters* 30(2), pp. 97-98, 1994
- [13] A. C. Ludwig, "The definition of cross polarization", *IEEE Trans. Antennas Propagat.* AP-21(1), pp. 116-119, 1973
- [14] A. A. Kishk, Y. Yin, A. W. Glisson, "Conical dielectric resonator antennas for wide-band applications", *IEEE Trans. Antennas Propagat.* AP-50(4), pp. 469-474, 2002
- [15] K. W. Leung, "Conformal strip excitation of dielectric resonator antenna", *IEEE Trans. Antennas Propagat.* AP-48(6), pp. 961-967, 2000



Christophe Fumeaux received the diploma and Ph.D. degrees in physics from the Swiss Federal Institute of Technology (ETH) Zurich, Switzerland, in 1992 and 1997, respectively. His Ph.D. thesis on antenna-coupled infrared detectors was awarded the ETH Silver Medal of Excellence. From 1998 to 2000 he was post-doctoral researcher in infrared technology at the School of Optics (CREOL) of the University of Central Florida (UCF), Orlando. In 2000 he joined the Swiss Federal Office of Metrology in Bern, Switzerland, as a scientific staff member. Since 2001, he is a research associate at the Laboratory for Electromagnetic Fields and Microwave Electronics (IFH) at ETH Zurich. His current main research interest concerns computational electromagnetics in the time domain for numerical analysis of microwave circuits and antennas.



Dirk Baumann received the Dipl. Ing. degree in electrical engineering from the University of Karlsruhe, Germany, in 2001. Between Spring and Fall 2000 he did an internship at the Alaska SAR Facility (ASF) in Fairbanks, AK, working on the calibration of ASF's SAR processor. Currently he is working toward the Ph.D. degree in electrical engineering at the Laboratory for Electromagnetic Fields and Microwave Electronics (IFH), ETH Zurich, Switzerland. His research interests

include numerical methods with emphasis on time domain techniques and their application to general electromagnetic problems.



Rüdiger Vahldieck received the Dipl. Ing. and the Dr. Ing. degrees in electrical engineering from the University of Bremen, Germany, in 1980 and 1983, respectively.

From 1984 to 1986 he was a Postdoctoral Fellow at the University of Ottawa, Canada. In 1986 he joined the Department of Electrical and Computer Engineering at the University of Victoria, British Columbia, Canada, where he became a Full Professor in 1991. During Fall and Spring of 1992-'93 he was a visiting scientist at the "Ferdinand-Braun-Institut für Höchstfrequenztechnik" in Berlin, Germany. In 1997 he accepted an appointment as Professor for electromagnetic field theory at the Swiss Federal Institute of Technology, Zurich, Switzerland, and became head of the Laboratory for Electromagnetic Fields and Microwave Electronics (IFH) in 2003. His research interests include computational electromagnetics in the general area of EMC and in particular for computer-aided design of microwave, millimeter wave and opto-electronic integrated circuits.

Professor Vahldieck is a Fellow of the IEEE. He received the J.K. Mitra Award of the IETE (in 1996) for the best research paper in 1995, and was co-recipient of the outstanding publication award of the Institution of Electronic and Radio Engineers in 1983. Since 1981 he has published more than 230 technical papers in books, journals and conferences, mainly in the field of microwave CAD. He is the Past-President of the IEEE 2000 International Zurich Seminar on Broadband Communications (IZS'2000) and since 2003 President and General Chairman of the international Zurich Symposium on Electromagnetic Compatibility. He is a member of the editorial board of the IEEE Transaction on Microwave Theory and Techniques. From 2000 until 2003 he served as an Associate Editor for the IEEE Microwave and Wireless Components Letters and has now become the Editor-in-Chief effective Jan. 2004. Since 1992 he serves on the Technical Program Committee of the IEEE International Microwave Symposium, the MTT-S Technical Committee on Microwave Field Theory, and in 1999 on the TPC of the European Microwave Conference. From 1998 until 2003 Professor Vahldieck was the chapter chairman of the IEEE Swiss Joint Chapter on MTT, AP and EMC.